Applied Catalysis A, General 663 (2023) 119306

Contents lists available at ScienceDirect

Applied Catalysis A, General

journal homepage: www.elsevier.com/locate/apcata

Enhanced photocatalytic toluene oxidation on CN species modified TiO_2: Nitrogen doping state and anti-inactivation mechanism

Haiqin Wan [a], Xiaoshan Zeng [a], Bingqing Shi [a], Qiuhui Qian [b], Qing Tong [a], Weixin Zou [a,*], Bin Gao [c,d], Lin Dong [a]

[a] State Key Laboratory of Pollution Control and Resource Reuse, School of the Environment, Jiangsu Key Laboratory of Vehicle Emissions Control, Center of Modern Analysis, Nanjing University, Nanjing 210023, China
[b] National and Local Joint Engineering Laboratory of Municipal Sewage Resource Utilization Technology, School of Environmental Science and Engineering, Suzhou University of Science and Technology, Suzhou 215009, China
[c] Department of Civil and Environmental Engineering, Rensselaer Polytechnic Institute, Troy, NY 12180, USA
[d] Department of Agricultural and Biological Engineering, University of Florida, Gainesville, FL 32611, United States

ARTICLE INFO

Keywords:
Photocatalytic toluene degradation
Urea calcination
Interstitial nitrogen
Anti-inactivation mechanism

ABSTRACT

The photocatalytic oxidation of toluene is limited by low mineralization and inactivation. Cheap carbon and nitrogen (CN) species on TiO_2 provides an efficient strategy. CN species from the urea calcination *in situ* formed on TiO_2 were denoted as UTx (x = 0.5, 1, 2), and UT1 photocatalyst had the best performance of *ca.* 90% conversion and 85% mineralization of toluene in light ($\lambda \geq 400$ nm, RH= 20%), with keeping for at least 720 min. The excellent activity of UT1 photocatalyst was resulted from the observed interstitial nitrogen and CN species with triple bonds. Because easily forming interstitial nitrogen resulted in isolated states and more negative VBM to generate hydroxyl radicals, and CN species with triple bonds was beneficial for transferring electrons and opening benzene rings. Therefore, quinone intermediates on UT1 were oxidized to 3-hydroxyglutaric dialdehyde and deeply mineralized, while more accumulated benzaldehyde on TiO_2 led to poorer stability.

1. Introduction

Volatile organic compounds (VOCs) are harmful to the human health, and the applications of photocatalytic technologies in the removal of indoor VOCs pollutants are gradually being valued by researchers [1,2]. Toluene is one of well-known VOCs pollutants in air, and the photocatalytic oxidation of toluene is attracted more attention and widely investigated [3–8].

Titanium dioxide (TiO_2) is a promising photocatalyst due to its excellent activity and cheap cost, which is widely used in various photocatalytic fields [9–13], such as VOCs degradation, water splitting, CO_2 reduction, waste water treatment, recovery of precious metals, *etc.* In the photocatalytic oxidation of toluene, the photo-generated charges and strong oxidizing radicals can be formed on TiO_2 under the UV irradiation, which decompose toluene to non-toxic molecules [14–16]. However, the large-scale application of TiO_2 in photocatalytic oxidation of toluene is restricted, because of the following shortcomings: (1) the band structure limits the visible light absorption; (2) the recombination rate of photogenerated electrons and holes is rapid; (3) toxic intermediates accumulation on the catalyst lead to the deactivation. Many strategies have been developed, such as doping metallic/nonmetallic elements, fabricating heterojunctions, depositing noble metals, and so on [15–19]. An efficient method is reported to modify TiO_2 by carbon-based materials. For example, the rGO with π-rings could provide sites for VOCs adsorption on TiO_2 [20]. Carbon quantum dots decorating TiO_2 could accelerate the separation of photo-generated charges [21].

The precursor of urea is reported to a potential material to form carbon and nitrogen species to promote properties of pure TiO_2, such as visible light absorption, photo-generated charge separation, catalytic performance, *etc.* [22–26] For example, Mitoraj and Kisch [23,24] proposed that the triazine ring structures from the thermal decomposition of urea replaced hydroxyls on TiO_2 surface, leading to the enhanced catalytic activity under visible light. The melon species was also suggested to generate from the co-thermal decomposition of urea on TiO_2 [25]. In addition, a small amount of carbon film and triazine rings from the urea decomposition were proposed to decorate TiO_2 [26]. However, the explicit structures of carbon and nitrogen species from thermal decomposing of urea on TiO_2 are unclear and inconsistent, further the

* Corresponding author.
E-mail address: wxzou2016@nju.edu.cn (W. Zou).

https://doi.org/10.1016/j.apcata.2023.119306
Received 16 April 2023; Received in revised form 14 June 2023; Accepted 15 June 2023
Available online 20 June 2023

roles of the existing forms of carbon and nitrogen species in the performance and mechanism of photocatalytic toluene oxidation on TiO_2 are worthy of study.

In the work, carbon and nitrogen species from the thermal decomposing of urea were employed to modify TiO_2, denoting as UTx (*x* were the mass ratios of urea precursor to TiO_2, *i.e.*, 0.5, 1, 2). Their photocatalytic activities and stabilities of toluene oxidation under light irradiation ($\lambda \geq 400$ nm) and a relative humidity of 20% were determined. The UT1 photocatalyst had the best toluene mineralization, and kept stable for at least 720 min. The mechanisms of enhanced mineralization and stability were explored. Characterizations of FT-IR, XRD, XPS, water contact angle, UV–vis DRS, and DFT calculations showed the existing forms of carbon and nitrogen species, which had influences on band structures, active radicals, and photo-generated electron transfer. In addition, DFT calculations, *in situ* DRIFTS of toluene adsorption under light irradiation, and GC-MS results investigated the reaction intermediates, and the possible reaction mechanism of toluene mineralization on UT1 was proposed. Furthermore, the fresh and used photocatalysts were analyzed to explain better stability of UT1 photocatalyst. This work provides a valuable guidance for the application of TiO_2-based photocatalysts in VOCs degradation.

2. Experimental section

2.1. Material

Urea and TiO_2 anatase nanoparticles were purchased from Maclin Reagent Co., Ltd. (China). All reagents were analytical pure without further treatment.

2.2. Photocatalyst synthesis

The 2 g of TiO_2 anatase nanoparticles and the urea precursor with different contents were mixed and milled evenly, then the mixture was transferred to a crucible with aluminum foil sealed. The crucible was calcined at 550 ℃ for 4 h with a heating rate of 5 ℃/min in an air atmosphere. Finally, the obtained samples were denoted as UTx, and *x* were the mass ratios of urea precursor to TiO_2, *i.e.*, 0, 0.5, 1, 2. The schematic diagram of UTx synthesis was showed in Fig. S1 of supporting information. In addition, the g-C_3N_4 sample was synthesized by heating urea precursor at 550 ℃ for 4 h with a heating rate of 5 ℃/min in a muffle furnace, and the obtained g-C_3N_4 was denoted as CN sample in the following discussion.

2.3. Characterization of photocatalysts

The crystal structures were measured by X-ray diffraction (XRD) with Philips X'Pert-Pro diffractometer by Cu Kα radiation ($\lambda = 0.15418$ nm). Transmission electron microscopy (TEM) images were obtained on the JEM-2100 instrument at an accelerating voltage of 200 kV. The samples were pretreated by crushing and dispersing in the A.R. grade ethanol, and the resulting suspensions were dried on carbon film supported copper grids. X-ray photoelectron spectroscopy (XPS) analysis was performed on the PHI 5000 VersaProbe high performance electron spectrometer with an Al Kα radiation (1486.6 eV) achromatic X-ray source. The samples were outgassed at room temperature in a UHV chamber. The charging effect of samples was compensated with C1s peak at 284.6 eV based on the adventitious carbon. The FT-IR spectra were measured from 400 to 4000 cm^{-1} on the Nicolet 5700 FT-IR spectrometer. The 5 mg of samples were mixed with the reagent of KBr and pressed into self-supported films. UV–vis diffuse reflectance spectroscopy (UV–vis DRS) were recorded from 200 to 800 nm by a Shimadzu UV 3600 spectrophotometer with the support of ultra-fine $BaSO_4$. Photoluminescence (PL) spectra were determined on the Fluoromax-4 fluorescence spectrophotometer and recorded from 360 to 800 nm. The electron spin resonance (ESR) measurements were obtained on a JEOL Co. spectrometer with the 5,5-dimethyl-1-pyrroline-N-oxide (DMPO) solvent. The photoelectrochemical measurements were carried out on a CHI660E electrochemical workstation system adopting a standard three-electrode cell. The photocatalytic materials were deposited on fluorine-doped tin oxide as the working electrode, with a platinum wire and Ag/AgCl electrode as the counter and reference electrodes, respectively. The electrolyte solution was Na_2SO_4 (0.1 M) and light source was a Xe lamp. The photocurrent response was measured at 0.5 V *vs* Ag/AgCl during the on-off cycles of 60 s under illumination. The electrochemical impedance spectroscopy (EIS) was tested at −0.6 V (*vs.* Ag/AgCl) from 10^5 to 0.1 Hz with a modulation amplitude of 20 mV. *In situ* diffuse reflectance infrared Fourier transform spectra (DRIFTS) were collected and determined on a Nicolet Nexus 5700 FT-IR spectrometer using the MCT detector. The *in situ* DRIFTS with the resolution of 4 cm^{-1} were carried out in a condition of 300 W Xenon lamp irradiation ($\lambda \geq 400$ nm) and toluene gas balanced by high purity air.

2.4. Photocatalytic oxidation of toluene

The photocatalytic experiment of toluene oxidation was carried out in a reactor, with a light source of a 300 W Xe lamp ($\lambda \geq 400$ nm). The 50 mg of photocatalyst was uniformly dispersed on the 304 stainless steel mesh. The toluene reactant gas was flowed by the high-purity air (21% O_2, N_2 balanced) into the reactor with a relative humidity of 20%. After adsorption of toluene in dark for 40 min, the photocatalytic performance of toluene oxidation under the light irradiation (($\lambda \geq 400$ nm) was determined. The schematic diagram of the photocatalytic toluene oxidation was showed in Fig. S2. The GC-MS analysis was described as followed. The used catalyst was added to 2 mL of ethyl acetate, afterward the above suspension was ultrasonicated for 30 min to dissolve the surface materials. Subsequently, the filter liquide from the suspension was further analyzed by GC-MS spectrometer (GC-MS, ISQ, Thermo), in the condition of pure helium gas as the mobile phase.

2.5. DFT calculations

The spin-polarized density functional theories (DFT) were performed by using the Vienna Ab initio Simulation Package (VASP) [27]. The Perdew-Burke-Ernzerhof generalized-gradient approximation functional was used to describe the interaction between electrons [28]. The energy cutoff was set to 400 eV. Monkhorst-Pack k-points of $3 \times 5 \times 1$ for the slab calculations. The vacuum region was set to be 15Å in z direction to prevent the interaction between two adjacent surfaces. The energy convergence and atomic forces were set to 10^{-5} eV and 0.02 eV/Å. HSE06 functionals were used to calculate the band structure [29].

The formation energy (E_f) for the incorporation was calculated as: $E_f = E_{total} - E_{TiO2} - E_N$, and the formation energy for the substitutional N-doped TiO_2(101) was calculated as: $E_f = E_{total} - E_{TiO2} - E_N + E_O$, where E_{total} and E_{TiO2} were the total energies with and without single N decoration, E_N and E_O were the energies of single N and single O atom, respectively [30].

3. Results and discussion

3.1. Photocatalytic performances of toluene oxidation

The photocatalytic toluene oxidation under a Xe lamp irradiation ($\lambda \geq 400$ nm, RH= 20%) was carried out, and the corresponding performances were displayed in Fig. 1. The conversion efficiencies of photocatalytic toluene oxidation were ordered by UT1 > UT0.5 > TiO_2 > UT2 > CN, and the sequence of mineralization was UT1 > UT0.5 > UT2 > TiO_2, which showed that TiO_2 was beneficial for toluene conversion, but the further mineralization was poor. The CN

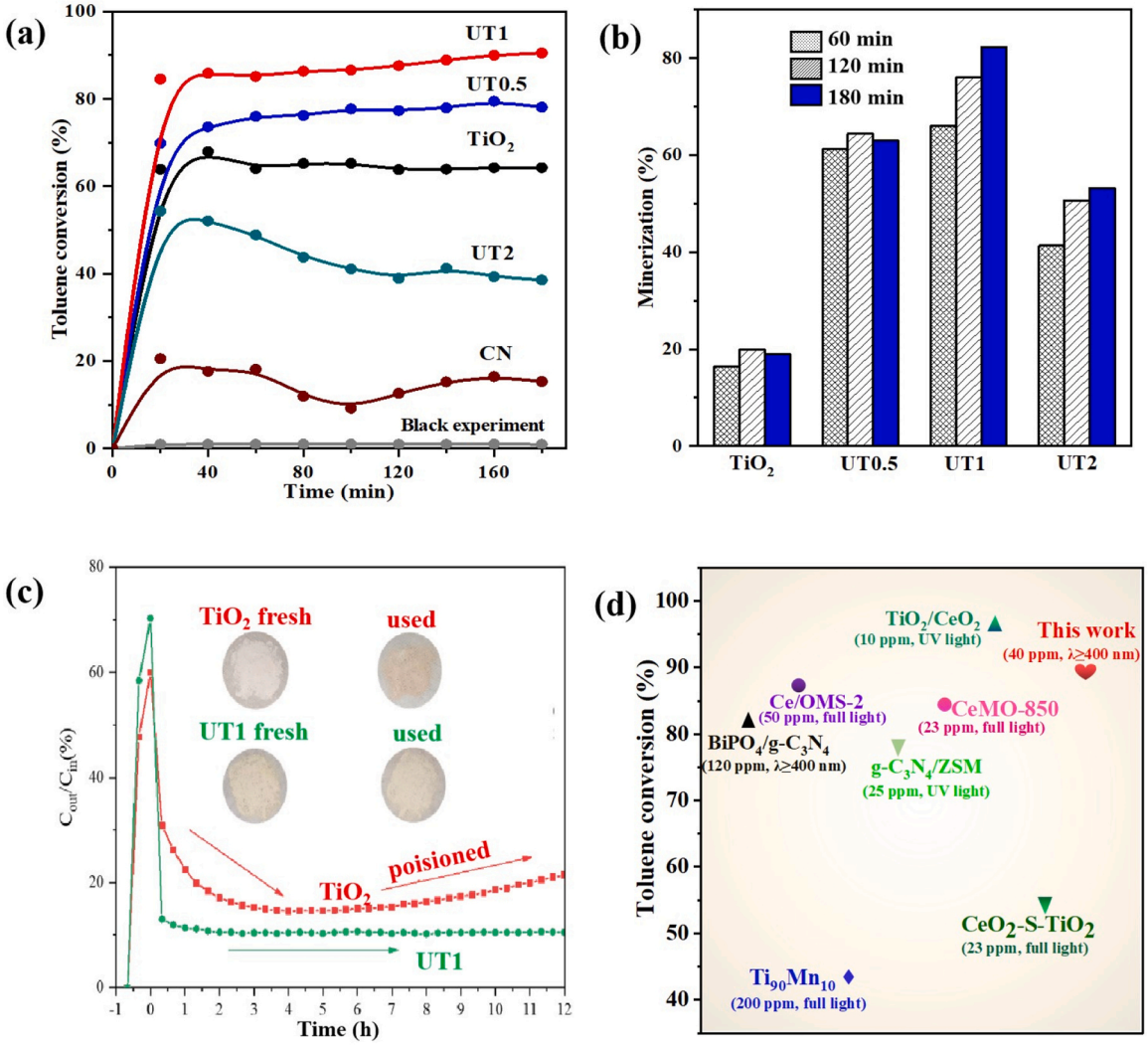

Fig. 1. (a) Photocatalytic activities of toluene oxidation, and (b) mineralization performances of TiO_2 and UTx. (c) Toluene conversions of TiO_2 and UT1 in 12 h under light irradiation ($\lambda \geq 400$ nm, RH= 20%). (d) Comparison of performances of photocatalytic toluene oxidation in literatures.

species calcined from urea precursor could improve the above shortcoming of TiO_2, and the mineralization rate was four times on UT1 sample than that of pure TiO_2. However, too more CN species on UT2 led to the decreased photocatalytic activity of toluene conversion. Subsequently, the stability test was carried out to confirm the advantage of UT1 sample. For 12 h (Fig. 1**c**), TiO_2 was gradually deactivated with the reaction process, while UT1 still maintained stable. Furthermore, the color of used TiO_2 became from white to yellow, whereas no obvious color change was on UT1 photocatalyst. In addition, the performance of photocatalytic toluene oxidation on UT1 catalyst was compared with that in literatures [31–37] (Fig. 1d), which showed that the UT1 catalyst had better and comparable activity.

Therefore, the UT1 photocatalyst was more beneficial for the oxidation and mineralization of toluene than pure TiO_2 and g-C_3N_4 (CN) samples. Why did the CN species on TiO_2 have influences on the toluene mineralization and stability? The existing forms of CN species from urea precursor, and the corresponding influences on the enhanced photoelectric properties and mineralization mechanisms were investigated.

3.2. *Existing forms of CN species*

The contents of carbon and nitrogen of UTx samples were detected by elemental analysis in Table S1, and the existing forms of CN species from urea precursor on UTx were investigated by the characterizations of TEM, XRD, water contact angles, XPS, FT-IR, and DFT calculations. TEM and HRTEM images showed the morphologies and nanostructures of TiO_2 and UT1 in Fig. S3a-d. It could be found that the particle sizes of TiO_2 and UT1 were *ca.* 15 nm, both TiO_2 and UT1 samples were possessed with the similar morphologies, and there was no obvious difference between TiO_2 and UT1. Furthermore, the lattice fringes of the as-synthesized TiO_2 and UT1 were determined, and both of them were 0.35 nm, corresponding to the anatase TiO_2 (101) crystal plane.

In addition, the phase structures of as-synthesized pure TiO_2, UT0.5, UT1, and UT2 photocatalysts were investigated by the XRD characterization. In Fig. 2b, the peaks of 2θ degree at 25.3°, 38.2°, 48.1° were attributed to (101), (004), (002) planes of anatase TiO_2 [38], respectively. Except for the TiO_2 anatase, no other peaks were observed on UTx, which suggested that the CN species led to no phase transformation of TiO_2 anatase, consistent with the results of HRTEM. On CN sample, the characteristic diffraction peak at 27.5° was attributed to g-C_3N_4 (002) plane [39], which were not found on UTx samples, and it is might be resulted from their low content or absence of g-C_3N_4. Furthermore, for the peak at *ca.* 25.3° of TiO_2 (101), compared with pure TiO_2, the peak of UTx samples shifted to a lower diffraction position. According to the reported literature [40], because the ionic radius of N^{3-} (0.171 nm) is larger than that of O^{2-} (0.140 nm), the lattice expansion would be generated by doping N. The increased water contact angles of UT1 also suggested the presence of doping N (Fig. 2**d**). Because lower water

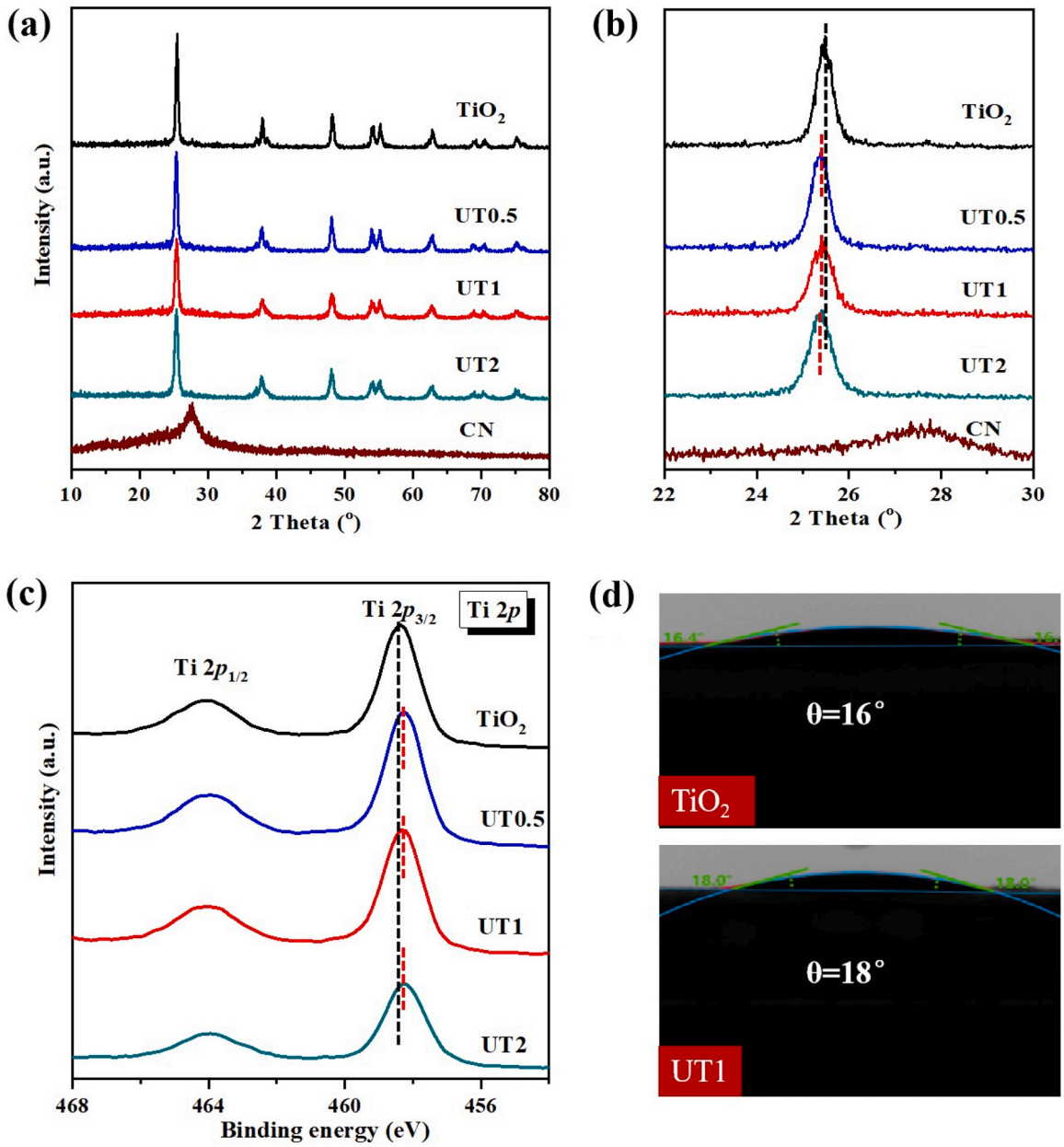

Fig. 2. (a) XRD patterns, (b) the magnified patterns of 22–30°, (c) XPS spectra of Ti 2*p* of as-prepared TiO_2 and UTx, and (d) water contact angles of TiO_2 and UT1.

contact angles suggest better hydrophilicity of the sample. Accordingly, the UT1 sample was provided by poorer hydrophilicity than TiO_2, due to the hydrophobic N dopant. On the basis of XRD patterns and water contact angles, it could be proposed that N species had been doped into TiO_2.

Generally, the ways of doping N are included of substitutional and interstitial forms. Therefore, the XPS characterization and DFT calculation were introduced to investigate the existing forms of N doping in UTx samples. The electronic states of UTx and TiO_2 were investigated by the Ti 2*p* XPS spectra. In Fig. 2**c**, there were two peaks at the binding energies of 464.3 −464.5 eV and 458.5 −458.8 eV, which were assigned to the spin−orbit splitting of Ti $2p_{1/2}$ and $2p_{3/2}$, respectively [41]. Compared with the pure TiO_2, the peaks attributed to Ti $2p_{3/2}$ were shifted to lower binding energies on UTx samples, indicating that the electron densities on Ti were increased [42]. The electronegativity of O atom is stronger than that of N atom, according to this point, interstitial N dopant, not substitution, was more facilitated to provide electrons to Ti.

Furthermore, the formation energies of interstitial and substitutional N doping into anatase TiO_2 (101) were calculated by DFT methods. In Fig. 3**a**, the energies of pure anatase TiO_2 (101), interstitial N-TiO_2 (101), and substitutional N-TiO_2 (101) were calculated, *i.e.*, −416.684, −420.437, and −415.094 eV, respectively. According to the calculation formula in the experimental section, the formation energies (E_f) of interstitial and substitutional N-TiO_2 (101) were −0.64 and 3.19 eV, respectively. It was found that E_f of the interstitial N-TiO_2 (101) was lower, and the interstitial N dopant was more facilitated to form, consistent with the XPS result.

Besides the presence of interstitial doping N, the other CN species on UTx were determined by the characterizations of FT-IR, XPS spectra of C 1 *s* and N 1 *s*. In Fig. 3**b**, for the CN sample, a broad band located at *ca.* 3600–3000 cm^{-1} was attributed to the absorbed hydroxyl and amino groups, and peaks in the region of 1600–1200 cm^{-1} were the characteristic vibration modes of aromatic C–N heterocycles and C═N species, with the sharp peak at around 804 cm^{-1} of the s-triazine unit of g-C_3N_4 [43,44]. In comparison with CN and UTx, it was observed that there

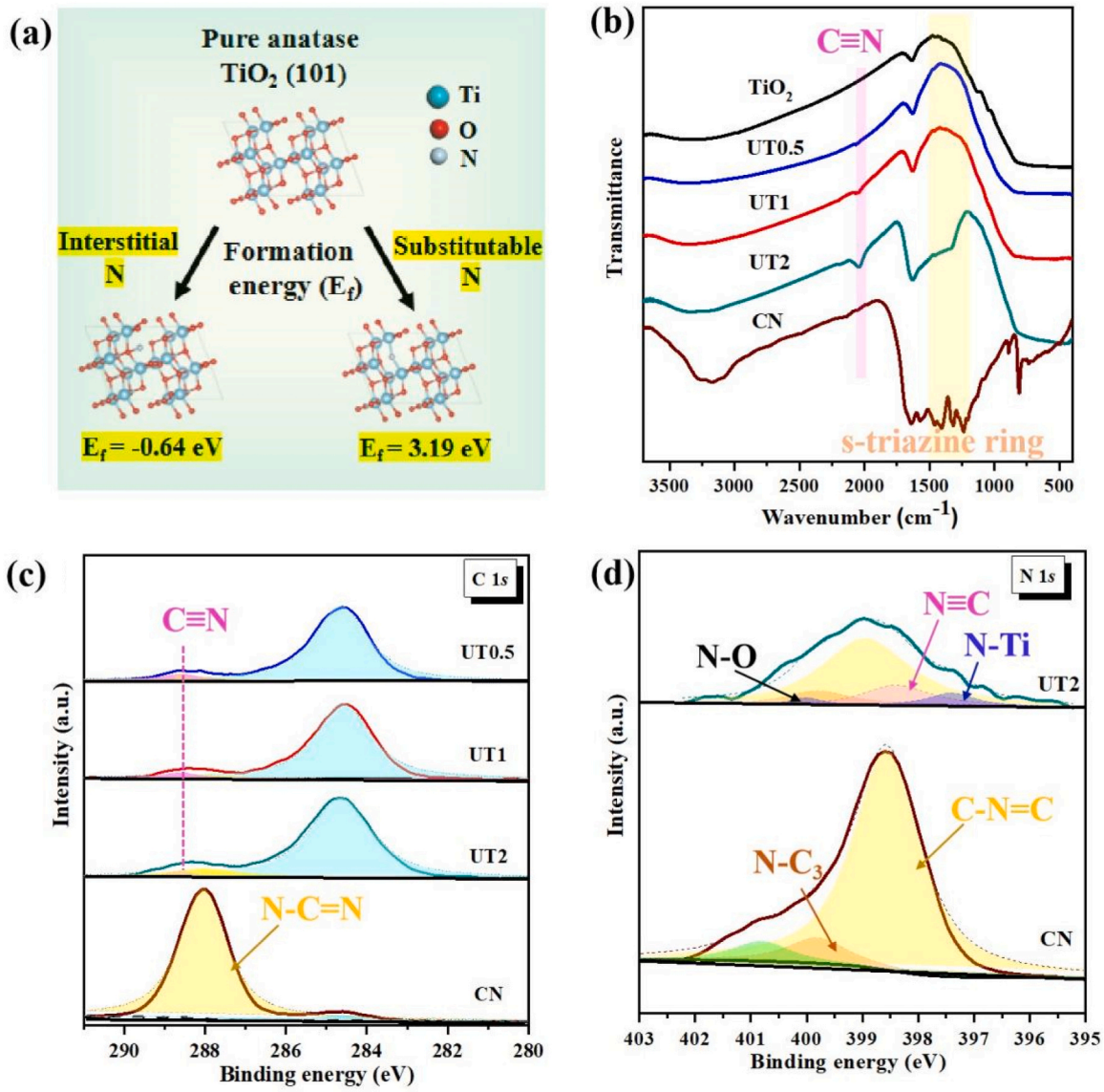

Fig. 3. (a) The formation energies of interstitial and substitutional and N doping into anatase TiO_2 (101). (b) FT-IR spectra, and XPS spectra of (c) C 1 *s* and (d) N 1 *s* of TiO_2 and UTx.

were no obvious peaks attributed to C–N heterocycles, C═N species, and s-triazine unit of g-C_3N_4 on UT0.5 and UT1. While, for UT2, with the further increased content of urea precursor, the peak intensity in the region of 1600–1200 cm^{-1} became intensive, indicating that aromatic C–N heterocycles and C═N species belonged to g-C_3N_4 generated on UT2. Interestingly, a new sharp peak at *ca.* 2150 cm^{-1} for C≡N triple bond appeared in UTx, not observed on CN and TiO_2 samples, suggesting that besides the interstitial doping N, C≡N species with triple bonds were on UTx samples.

XPS spectra of C 1 *s* and N 1 *s* were used to confirm the existing of C≡N species with triple bonds on UTx. In Fig. 3**c**, according to literatures [45,46], in the XPS spectra of C 1 *s* of CN sample, the peaks at *ca.* 288.0 and 284.6 eV were attributed to the sp^2-bonded carbon atom in aromatic rings (N = C═N) of g-C_3N_4 and carbon contamination, respectively. Compared with UTx, it was found that a fitted peak at *ca.* 288.3 eV was generated, which were shifted to higher binding energies than the signal of N = C═N species. Because the electronegativity of N is larger than that of C atom, combined with the FT-IR result, the peak was attributed to C≡N species with triple bonds. In addition, the spectra of N 1 *s* in Fig. 3**d** also showed the presence of C≡N species with triple bonds. The peaks at *ca.* 398.4 and 399.7 eV were assigned to the sp^2-hybridized (C═N = C) nitrogen atom and tertiary nitrogen (N–C_3) on g-C_3N_4, respectively [47,48]. Due to the low N concentration or N doping into bulk of UT1, its N 1 *s* spectrum was hard to fit. Therefore, the broad peak of N 1 *s* in UT2 was replaced. As for the broad peak, it was fitted into peaks at 398.5, 399.7, 398.0, 397.0, and 400.0 eV [47–49]. Except for the C═N = C (398.5 eV) and N–C_3 (399.7 eV) of g-C_3N_4, the signals at 398.0 eV for CN species with triple bonds, 397.0 eV and 400.0 eV for N-Ti and N-O were observed, respectively.

On the basis of the above results, it could be proposed that the existing forms of CN species were interstitial doping N, C≡N species with triple bonds, and g-C_3N_4. Interstitial N and C≡N species were on all UTx samples, while g-C_3N_4 species was only on UT2 sample with the increased content of urea precursor.

3.3. *Active radicals*

Generally, the deep oxidation and mineralization of photocatalytic toluene are attributed to active radicals, the *in situ* ESR characterizations were carried out to determine the active radicals. In Fig. 4**a, b**, for TiO_2

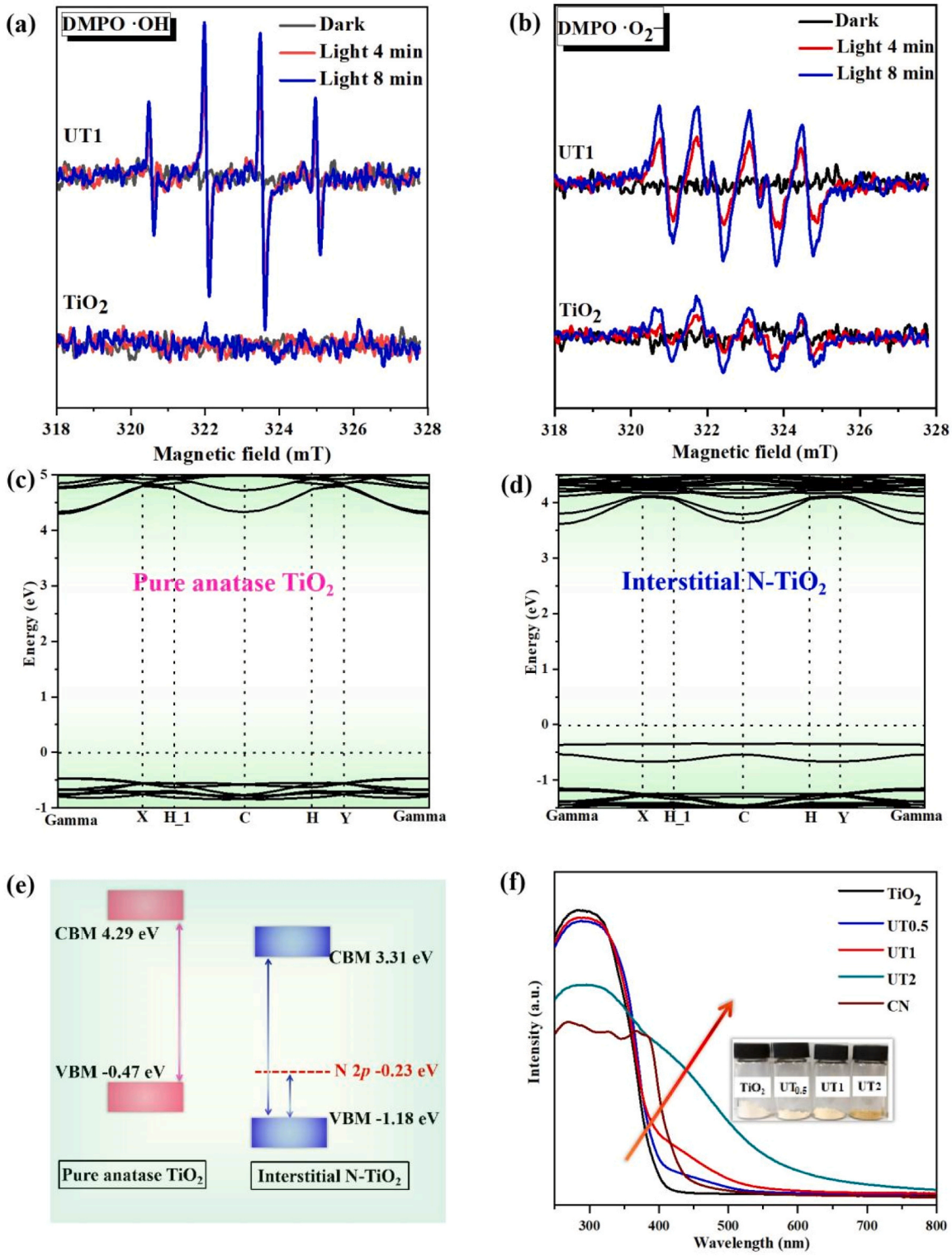

Fig. 4. ESR spectra of TiO_2 and UT1 for (a) DMPO-•OH, and (b) DMPO-•O_2^- under visible light irradiation. Band structures from DFT calculation of (c) pure anatase TiO_2, (d) interstitial N-TiO_2, (e) the schematic diagram of band gaps of pure anatase TiO_2 and interstitial N-TiO_2. (f) UV–vis DRS spectra of UTx and TiO_2.

and UT1, the active radicals in the dark were almost negligible, and the hydroxyl (•OH) and superoxide (•O_2^-) radicals were increased with the light irradiation. Richer active radicals were generated on UT1, while fewer were found on TiO_2 under visible light irradiation, which were related to the band structures and photo-generated charges, resulting from the existing of CN species. Therefore, the DFT calculations and UV–vis DRS characterization were carried out to analyze the band structures.

The band structures of pure anatase TiO_2 and interstitial N-TiO_2 were calculated in comparison, based on easily formed interstitial N dopant (Fig. 3a). The valence band (VB) consists of Ti 3*d* and O 2*p* orbitals, and the conductive band (CB) is mainly Ti 3*d* states. In Fig. 4c and d, the VB position was below the Fermi level (E = 0 eV), and CB was above. In interstitial N-TiO_2, owing to electronic interactions of interstitial N-

TiO_2, the isolated N 2*p* states (−0.23 eV) were found lying at the top of VBM, which could act as transfer stations for photo-generated charges [50], leading to more available photoelectrons for active radicals. In addition, the electronic interactions of interstitial N-TiO_2 resulted in more negative VBM energy (−1.18 eV) than TiO_2 (−0.47 eV), leading to richer •OH generation (Fig. 4e). The UV–vis DRS spectra also confirm the above band structures. In Fig. 4f, for TiO_2, only the absorption of around 400 nm was observed, while for UT0.5 and UT1, another absorption region of 400–500 nm was generated, according to the DFT calculations, the tailing was attributed to the presence of mid-gap levels in the band gap of interstitial N doping. In addition, the narrower band gap of UT2 was found, because of a formed heterojunction of TiO_2 and g-C_3N_4, consistent with the result of FT-IR spectra. The band energies from UV–vis DRS were moderately consistent with theoretical band gaps, which were ascribed to the unknown exchange−correlation energy from the restriction of DFT calculations [51]. Therefore, in UT1 photocatalyst, interstitial N species led to the formation of isolated N 2*p* states on the VBM position, which kinetically and thermodynamically generated richer active radicals, respectively.

In addition, faster photo-generated charge transfer is beneficial for more active radicals, and photoelectric properties were carried out by PL spectra and transient photocurrent responses. PL spectra show the recombination rates of photo-generated electrons and holes, and stronger fluorescence signal often suggests faster recombination rates [52,53]. In Fig. S4a, the emission spectra of TiO_2, UT0.5 and UT1 exhibited similar the peak shape, whereas with the increased calcined urea content, the peak shape of UT2 changed, which was similar to g-C_3N_4. The phenomenon indicated that different CN species were on UTx, consistent with the results of XPS, FT-IR and UV–vis DRS. Furthermore, the PL emission peak intensity of UT1 was weaker than other UTx and TiO_2, suggesting the efficient suppressing recombination of photo-generated electrons and holes on UT1. The transient photocurrent responses ran five on-off cycles in Fig. S4b. The photocurrent response intensities were ordered by UT1 > UT0.5 > TiO_2 > UT2 > g-C_3N_4. Generally, stronger photocurrent response means faster transfer of photo-generated charges. Therefore, UT1 had the excellent performance in photo-generated charge separation. Combined with the results of FT-IR, XPS, and DFT calculations, UT1 photocatalyst had a lower recombination of photo-generated charges, because C≡N species acted as transfer sites of photo-generated charges. In a word, richer •OH and $\bullet O_2^-$ radicals forming in UT1 were closely related to the interstitial N and C≡N species, under the above synergistic effects, UT1 was provided with more active radicals to deeply mineralize toluene and enhance the stability.

Moreover, the fresh and used UT1 and TiO_2 photocatalysts were characterized by PL, FT-IR, UV–vis DRS to further confirm better stability of UT1. After photocatalytic toluene oxidization for 12 h, the photoelectric properties of fresh and used TiO_2 photocatalysts were obviously different. In Fig. S5a, the PL intensity of the used TiO_2 was more intensive than the fresh one, while no obvious change between the fresh and used UT1. In addition, the UV–vis DRS spectra also changed (Fig. S5b). For the used TiO_2, the visible absorption appeared, due to benzene-containing reaction intermediates accumulation on the used TiO_2. Whereas, the light absorption of the fresh and used UT1 were unchanged, indicating a better stability of UT1. Furthermore, in the FT-IR spectra of the used TiO_2, a new peak at around 1700 cm^{-1} appeared (Fig. S5c), attributed to the signal of C=O [54]. Whereas, the FT-IR spectra of the fresh and used UT1 had no changes, indicating no obvious reaction intermediates poisoning UT1 surface (Fig. S5d). On the basis of that, it could be proposed that UT1 with the interstitial N and C≡N species could generate more active radicals to deeply mineralize toluene and had better stability than TiO_2.

3.4. Reaction mechanisms

The *in situ* DRIFTS of toluene adsorption in dark or light were determined to investigate the adsorption, activation, and reaction pathways on TiO_2 and UT1. In Fig. S6, the adsorption bands at 1654, 1537, 1500–1250 cm^{-1} were attributed to adsorbed toluene, as well as 2900–3500 cm^{-1} for benzyl group and 3500–4000 cm^{-1} for hydroxyl [55,56]. There was more intensive peaks on TiO_2 than UT1, indicating that TiO_2 had better hydrophily observed in the result of water contact angles, and thus the toluene was easier to adsorb on TiO_2, due to hydroxyls on TiO_2 interacting with methyl groups of toluene through hydrogen bondings [33,57]. Subsequently, *in situ* DRIFTS of photocatalytic toluene oxidation in light were showed in Fig. 5. With the increased irradiation time, new intermediates including of phenylic C-H stretching vibrations of aromatic ring (3487–2973 cm^{-1}), symmetric and antisymmetric C-H stretching vibrations of CH_2 group in benzyl species (2952, 2897 cm^{-1}), C=O stretching vibrations of benzaldehyde (1654 cm^{-1}), C=C vibrations of olefins (1600 cm^{-1}), C=C vibrations of benzene ring (1510 cm^{-1}), tertiary alcohol (1300 cm^{-1}), and benzyl alcohol (1094 cm^{-1}) [58–60] were observed. On TiO_2 surface, a great number of benzyl alcohol and benzaldehyde intermediates accumulated. While, for UT1, the signal of above intermediates was decreased, ring opening intermediates were generated with the light irradiation, including of olefins and tertiary alcohol. The different intermediates of photocatalytic toluene degradation showed that UT1 had better ability of oxidation and mineralization, which were related with its richer active radicals.

Furthermore, the GC-MS spectra were used to determine the key ring opening intermediates, and explore the degradation pathway of photocatalytic toluene [61]. According to the retention time and mass-to-charge ratio, the molecular formula and possible intermediates of photocatalytic toluene oxidization were analyzed in Table S1. The retention times of 6.78, 9.02, 9.59, 13.62, 20.24 min were ascribed to toluene, quinone, 3-hydroxyglutaric dialdehyde, benzaldehyde, benzoic acid, respectively. In Fig. 5**e**, in the gas phases, the signal of toluene was observed on TiO_2 and UT1, and the benzaldehyde intermediate species also was present in the gas, which was richer on TiO_2 than UT1. In addition, reaction intermediates on the photocatalyst surface were determined. In Fig. 5**f**, the toluene, benzaldehyde, and benzoic acid intermediates were on both TiO_2 and UT1 surfaces, and compared with the intensities of peaks of benzaldehyde and benzoic acid, more benzoic acid was on UT1 surface, indicating of its excellent oxidation ability, consistent with the *in situ* DRIFTS in light. Moreover, important ring-opening intermediates of 3-hydroxyglutaric dialdehyde from quinone was generated on UT1 surface, showing its best mineralization ability.

On the basis of *in situ* DRIFTS and GC-MS spectra, the degradation pathway of photocatalytic toluene was proposed in Fig. 6 as followed: (1) the methyl of toluene interacted with the hydroxyl on TiO_2 surface with hydrogen bonding, the activated methyl of toluene was oxidized by $\bullet O_2^-$ to benzaldehyde. (2) Under the attack of •OH, the oxidation of carbonyl to carboxyl generated benzoic acid. Due to fewer •OH on TiO_2, more benzaldehyde, not benzoic acid were found. (3) The ortho hydrogen atom of the benzoic acid was active, which were attacked by the C≡N species on UT1 surface with π electrons. Under the interaction of •OH and $\bullet O_2^-$, the quinone intermediate generated, and opened rings to 3-hydroxyglutaric dialdehyde. (4) The carbon chain was broken into acetone intermediate, which further oxidized to CO_2. Owing to the intensive electronic interactions of interstitial N species in UT1, its band structure was beneficial for active radical formation, and C≡N species was helpful for opening rings. Under the above advantages, UT1 had better mineralization and stability than TiO_2.

4. Conclusions

The UTx photocatalysts of CN species modifying TiO_2 were prepared to enhance the toluene mineralization and photocatalyst stability. UT1 had the best performance, because its interstitial N dopant and C≡N species resulted in more negative VBM and faster electron transfer for more radicals to open rings and mineralize toluene. Under the above

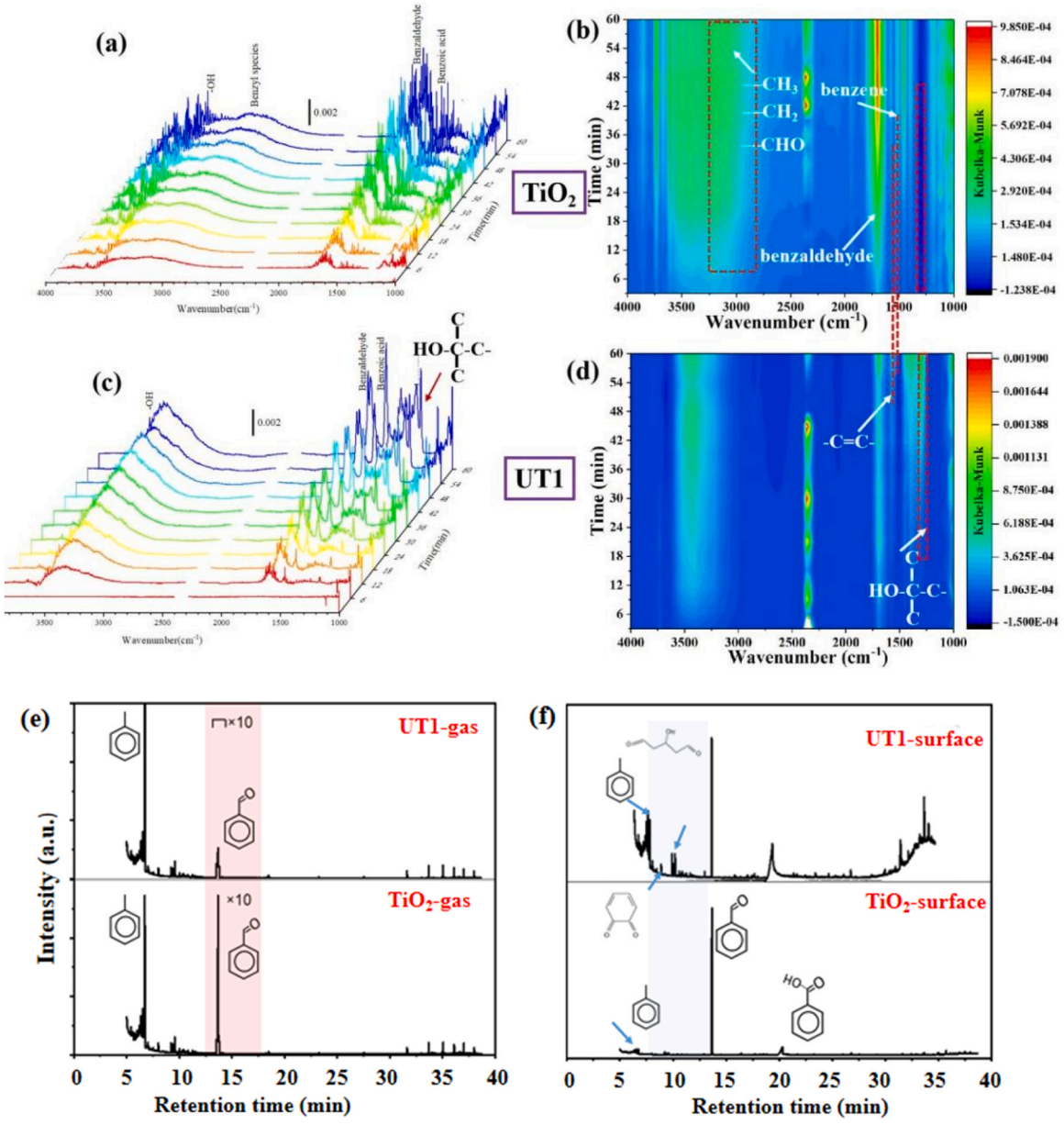

Fig. 5. *In situ* DRIFTS of photocatalytic toluene degradation on (a, b) TiO_2, and (c, d) UT1 in light irradiation within 60 min. GC-MS spectra of UT1 and TiO_2 photocatalysts: (e) in gas phases and (f) on surfaces after photocatalytic oxidation for 3 h.

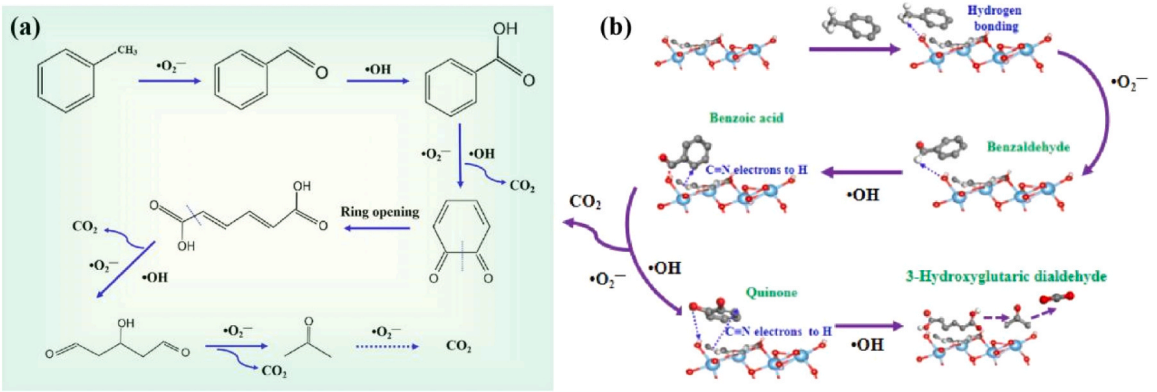

Fig. 6. (a) The degradation pathway of photocatalytic toluene, and (b) the possible schematic diagram on UT1 photocatalyst (red atom: oxygen, blue atom: Ti, gray atom: C, white atom: H).

synergistic effects, ring-opening intermediates of 3-hydroxyglutaric dialdehyde were observed on UT1, not TiO_2, which suggested that UT1 had better mineralization ability. This work provides a valuable guidance for the application of TiO_2-based photocatalysts in VOCs degradation.

CRediT authorship contribution statement

Haiqin Wan: Writing – original draft, Data curation. **Xiaoshan Zeng:** Investigation, Validation. **Bingqing Shi**: Methodology, Investigation. **Qinhui Qian**: Visualization. **Qing Tong**: Funding acquisition, Resources. **Weixin Zou**: Conceptualization, Writing – review & editing, Supervision. **Lin Dong**: Funding acquisition, Supervision.

Declaration of Competing Interest

The authors declare that they have no known competing financial interests or personal relationships that could have appeared to influence the work reported in this paper.

Data availability

Data will be made available on request.

Acknowledgements

The authors gratefully acknowledge the financial support from the National Natural Science Foundation of China (21976082, 22106067, 21972062).

Appendix A. Supporting information

Supplementary data associated with this article can be found in the online version at doi:10.1016/j.apcata.2023.119306.

References

[1] X.R. Li, Y. Chen, Y. Tao, L. Shen, Z.M. Xu, Z.F. Bian, H.X. Li, Challenges of photocatalysis and their coping strategies, Chem. Catal. 2 (2022) 1315–1345.
[2] X. Yue, N.L. Ma, C. Sonne, R. Guan, S.S. Lam, Q. Van Le, X. Chen, Y. Yang, H. Gu, J. Rinklebe, W. Peng, Mitigation of indoor air pollution: a review of recent advances in adsorption materials and catalytic oxidation, J. Hazard. Mater. 405 (2021), 124138. -124138.
[3] A. Enesca, C. Cazan, Volatile organic compounds (VOCs) removal from indoor air by heterostructures/composites/doped photocatalysts: a mini-review, Nanomaterials 10 (2020) 1965–1983.
[4] M.L. Deb, B.S. Saikia, I. Rahman, P.K. Baruah, Metal-free catalysis in C–C single-bond cleavage: achievements and prospects, Top. Curr. Chem. 380 (2022) 38.
[5] Y. Yang, S.H. Zhao, F.K. Bi, J.F. Chen, Y.X. Wang, L.F. Cui, J.C. Xu, X.D. Zhang, Highly efficient photothermal catalysis of toluene over Co_3O_4/TiO_2 p-n heterojunction: the crucial roles of interface defects and band structure, Appl. Catal. B: Environ. 315 (2022), 121550.
[6] Z.Y. Zhao, S.T. Ma, B. Gao, F.K. Bi, R. Qiao, Y. Yang, M.H. Wu, X.D. Zhang, A systematic review of intermediates and their characterization methods in VOCs degradation by different catalytic technologies, Sep. Purif. Technol. 314 (2023), 123510.
[7] F.K. Bi, Z.Y. Zhao, Y. Yang, N. Liu, Y.D. Huang, X.D. Zhang, Chlorine-coordinated Pd single atom enhanced the chlorine-resistance for volatile organic compounds degradation: mechanism study, Environ. Sci. Technol. 56 (2022) 17321–17330.
[8] Y. Yang, S.H. Zhao, F.K. Bi, J.F. Chen, Y.T. Li, L.F. Cui, J.C. Xu, X.D. Zhang, Oxygen-vacancy-induced O_2 activation and electron-hole migration enhance photothermal catalytic toluene oxidation, Cell Rep. Phys. Sci. 3 (2022), 101011.
[9] C. Song, L.F. Wang, F. Gao, Q.Y. Lu, Two-dimensional hollow TiO_2 nanoplates with enhanced photocatalytic activity, Chem. Eur. J. 22 (2016) 6368–6373.
[10] L. Zhou, M. Cai, X. Zhang, N. Cui, G. Chen, G.Y. Zou, In-situ nitrogen-doped black TiO_2 with enhanced visible-light-driven photocatalytic inactivation of Microcystis aeruginosa cells: synthesization, performance and mechanism, Appl. Catal. B: Environ. 272 (2020), 119019.
[11] D.W. Ma, J. Schneider, W.I. Lee, J.H. Pan, Controllable synthesis and self-template phase transition of hydrous TiO_2 colloidal spheres for photo/electrochemical applications, Adv. Colloid Interface Sci. 295 (2021), 102493.
[12] Y. Chen, S.H. Guan, H. Ge, X. Chen, Z.M. Xu, Y.L. Yue, H. Yamashita, H. Yu, H.X. Li, Z.F. Bian, Photocatalytic dissolution of precious metals by TiO_2 through photogenerated free radicals, Angew. Chem. Int. Ed. 61 (2022), e202213640.
[13] Y. Chen, M.J. Xu, J.Y. Wen, Y. Wan, Q.F. Zhao, X. Cao, Y. Ding, Z.L. Wang, H.X. Li, Z.F. Bian, Selective recovery of precious metals through photocatalysis, Nat. Sustain 4 (2021) 618–626.
[14] K.D. Kim, N.K. Dey, H.O. Seo, Y.D. Kim, D.C. Lim, M.Y. Lee, Photocatalytic decomposition of toluene by nanodiamond-supported TiO_2 prepared using atomic layer deposition, Appl. Catal. A Gen. 408 (2011) 148–155.
[15] (a) T.Z. Xu, H. Zheng, P.Y. Zhang, Isolated Pt single atomic sites anchored on nanoporous TiO_2 film for highly efficient photocatalytic degradation of low concentration toluene, J. Hazard. Mater. 388 (2020), 121746;
(b) H.A. Yurtsever, M. Ciftcioglu, The effect of rare earth element doping on the microstructural evolution of sol-gel titania powders, J. Alloy. Compd. 695 (2017) 1336–1353.
[16] (a) W.Q. Qu, P.L. Wang, M. Gao, J.Y. Hasegawa, Z. Shen, Q. Wang, R.M. Li, D. S. Zhang, Delocalization effect promoted the indoor air purification via directly unlocking the ring-opening pathway of toluene, Environ. Sci. Technol. 54 (2020) 9693–9701;
(b) L. Zeng, Z. Lu, M. Li, J. Yang, W. Song, D. Zeng, C. Xie, A modular calcination method to prepare modified N-doped TiO_2 nanoparticle with high photocatalytic activity, Appl. Catal. B Environ. 183 (2016) 308–316.
[17] T.D. Pham, B.K. Lee, Selective removal of polar VOCs by novel photocatalytic activity of metals co-doped TiO_2/PU under visible light, Chem. Eng. J. 307 (2017) 63–73.
[18] T.B. Lan, W.F. Zhang, N. Wu, M.D. Wei, Nb-doped rutile TiO_2 mesocrystals with enhanced lithium storage properties for lithium ion battery, Chem. Eur. J. 23 (2017) 5059–5065.
[19] J.J. Sun, X.Y. Li, Q.D. Zhao, O. Moses, S.M. Tadé, Liu, Quantum-sized $BiVO_4$ modified TiO_2 microflower composite heterostructures: efficient production of hydroxyl radicals towards visible light-driven degradation of gaseous toluene, J. Mater. Chem. A 3 (2015) 21655–21664.
[20] Z. Rao, G. Lu, A. Mahmood, G. Shi, X. Xie, J. Sun, Deactivation and activation mechanism of TiO_2 and rGO/Er^{3+}-TiO_2 during flowing gaseous VOCs photodegradation, Appl. Catal. B Environ. 284 (2021), 119813.
[21] A. Mahmood, G.S. Shi, Z. Wang, Z.P. Rao, W. Xiao, X.F. Xie, J. Sun, Carbon quantum dots-TiO_2 nanocomposite as an efficient photocatalyst for the photodegradation of aromatic ring-containing mixed VOCs: an experimental and DFT studies of adsorption and electronic structure of the interface, J. Hazard. Mater. 401 (2021), 123402.
[22] J.W. Xu, Y. Li, X.M. Zhou, Y.Z. Li, Z.D. Gao, Y.Y. Song, P. Schmuki, Graphitic C_3N_4-sensitized TiO_2 nanotube layers: a visible-light activated efficient metal-free antimicrobial platform, Chem. Eur. J. 22 (2016) 3947–3951.
[23] D. Mitoraj, H. Kisch, The nature of nitrogen-modified titanium dioxide photocatalysts active in visible light, Angew. Chem. Int. Ed. 47 (51) (2008) 9975–9978.
[24] D. Mitoraj, H. Kisch, On the mechanism of urea-induced titania modification, Chem. Eur. J. 16 (2010) 261–269.
[25] J. Pérez-Obando, D.A. Marín-Silva, A.N. Pinotti, L.R. Pizzio, P. Osorio-Vargas, J. A. Rengifo-Herrera, Degradation study of malachite green on chitosan films containing heterojunctions of melon/TiO_2 absorbing visible-light in solid-gas interfaces, Appl. Catal. B Environ. 244 (2019) 773–785.
[26] H. Zong, T. Zhao, G. Zhou, R. Qian, T. Feng, J.H. Pan, Revisiting structural and photocatalytic properties of g-C_3N_4/TiO_2: is surface modification of TiO_2 by calcination with urea an effective route to "solar" photocatalyst, Catal. Today 335 (2019) 252–261.
[27] G. Kresse, J. Furthmüller, Efficiency of ab-initio total energy calculations for metals and semiconductors using a plane-wave basis set, Comp. Mater. Sci. 6 (1996) 15–50.
[28] J.P. Perdew, K. Burke, M. Ernzerhof, Generalized gradient approximation made simple, Phys. Rev. L 77 (18) (1996), 3865-386.
[29] J. Heyd, G.E. Scuseria, M. Ernzerhof, Hybrid functionals based on a screened coulomb potential, J. Chem. Phys. 118 (2003) 8207–8217.
[30] Y.M. Liu, W. Liang, W., G. Zhang, J.J. Zhang, P. Han, First principle study of Cu–N, Cu and N-doped anatase TiO_2, Solid State Commun. 164 (2013) 27–31.
[31] P.P. Yu, N. Li, W.X. Zou, X.Q. Wei, J.W. Ji, L. Han, Y.D. Cai, W. Tan, B. Gao, L. Dong, K^+ and CeO_2 nanoparticles modified OMS-2 nanorods for enhanced activity and stability of photocatalytic toluene oxidation: K^+ charge modulation and mechanistic investigation, Chem. Eng. J. 451 (2023) 138943..
[32] M.C. Nevárez-Martínez, M.P. Kobylański, P. Mazierski, J. Wółkiewicz, G. Trykowski, A. Malankowska, M. Kozak, P.J. Espinoza-Montero, A. Zaleska-Medynska, Self-organized TiO_2-MnO_2 nanotube arrays for efficient photocatalytic degradation of toluene, Molecules 22 (2017) 564.
[33] X.Q. Wei, K. Li, X.Y. Zhang, Q. Tong, J.W. Ji, Y.D. Cai, B. Gao, W.X. Zou, L. Dong, CeO_2 nanosheets with anion-induced oxygen vacancies for promoting photocatalytic toluene mineralization: toluene adsorption and reactive oxygen species, Appl. Catal. B Environ. 317 (2022), 121694.
[34] V.B. Koli, J. Kim, Photocatalytic oxidation for removal of gases toluene by TiO_2-CeO_2 nanocomposites under UV light irradiation, Mat. Sci. Semicon. Proc. 94 (2019) 70–79.
[35] X.D. He, J.M. Zhu, L. Tan, H.M. Wang, M. Zhou, Visible light-induced photocatalytic degradation of gaseous toluene by Ce, S and N doped ionic liquid-TiO_2, Mat. Sci. Semicon. Proc. 120 (2020), 105259.
[36] D.H. Xia, W.J. Xu, L.L. Hu, C. He, D.Y.C. Leung, W.J. Wang, P.K. Wong, Synergistically catalytic oxidation of toluene over Mn modified g-C_3N_4/ZSM-4 under vacuum UV irradiation, J. Hazard. Mater. 349 (2018) 91–100.
[37] X.J. Zou, Y.Y. Dong, X.Y. Li, Q.D. Zhao, Y.B. Cui, G. Lu, Inorganic–organic photocatalyst $BiPO_4$/g-C_3N_4 for efficient removal of gaseous toluene under visible light irradiation, Catal. Commun. 69 (2015) 109–113.

[38] C. Zhang, Y.M. Zhou, Y.W. Zhang, S. Zhao, J.S. Fang, X.L. Sheng, T. Zhang, H. X. Zhang, Double-shelled TiO_2 hollow spheres assembled with TiO_2 nanosheets, Chem. Eur. J. 23 (2017) 4336–4343.
[39] W.Q. Li, L. Jin, F. Gao, H.Q. Wan, Y. Pu, X.Q. Wei, C. Chen, W.X. Zou, C.Z. Zhu, L. Dong, Advantageous roles of phosphate decorated octahedral CeO_2 {111}/g-C_3N_4 in boosting photocatalytic CO_2 reduction: charge transfer bridge and Lewis basic site, Appl. Catal. B Environ. 294 (2021), 120257.
[40] C. Han, J.J. Liu, W.J. Yang, Q.Q. Wu, H. Yang, X.X. Xue, Enhancement of photocatalytic activity of $CaTiO_3$ through HNO_3 acidification, J. Photoch. Photobio. A Chem. 322 (2016) 1–9.
[41] K.L. Tang, Z.Q. Wang, W.X. Zou, H.Y. Guo, Y.C. Wu, Y. Pu, Q. Tong, H.Q. Wan, X. R. Gu, L. Dong, J.F. Rong, Y.W. Chen, Advantageous role of Ir^0 supported on TiO_2 nanosheets in photocatalytic CO_2 reduction to CH_4: fast electron transfer and rich surface hydroxyl groups, ACS Appl. Mater. Interfaces 13 (5) (2021) 6219–6228.
[42] Z.C. Zhu, Q.M. Xian, Q.Y. He, C.X. Chen, W.X. Zou, C. Sun, S.B. Wang, X.G. Duan, Edge-rich bicrystalline 1T/2H-MoS_2 cocatalyst-decorated {110} terminated CeO_2 nanorods for photocatalytic hydrogen evolution, ACS Appl. Mater. Interfaces 13 (2021) 35818–35827.
[43] X.Q. Wei, X. Wang, Y. Pu, A.N. Liu, C. Chen, W.X. Zou, Y.L. Zheng, J.S. Huang, Y. Zhang, Y.C. Yang, Mu Naushad, B. Gao, L. Dong, Facile ball-milling synthesis of CeO_2/g-C_3N_4 Z-scheme heterojunction for synergistic adsorption and photodegradation of methylene blue: characteristics kinetics, models, and mechanisms, Chem. Eng. J. 420 (2021), 127719.
[44] W.X. Zou, B. Deng, X.X. Hu, Y.P. Zhou, Y. Pu, S.H. Yu, K.L. Ma, J.F. Sun, H.Q. Wan, L. Dong, Crystal-plane-dependent metal oxide-support interaction in CeO_2/g-C_3N_4 for photocatalytic hydrogen evolution, Appl. Catal. B Environ. 238 (2018) 111–118.
[45] J. Senthilnathan, L. Philip, Photocatalytic degradation of lindane under UV and visible light using N-doped TiO_2, Chem. Eng. J. 161 (1) (2010) 83–92.
[46] W.X. Zou, Y. Shao, Y. Pu, Y.D. Luo, J.F. Sun, K.L. Ma, C.J. Tang, F. Gao, L. Dong, Enhanced visible light photocatalytic hydrogen evolution via cubic CeO_2 hybridized g-C_3N_4 composite, Appl. Catal. B Environ. 218 (2017) 51–59.
[47] S. Yin, K. Ihara, M. Komatsu, Q. Zhang, F. Saito, T. Kyotani, T. Sato, Low temperature synthesis of $TiO_{2-x}N_y$ powders and films with visible light responsive photocatalytic activity, Solid State Commun. 137 (2006) 132–137.
[48] W.X. Zou, L.X. Xu, Y. Pu, H.J. Cai, X.Q. Wei, Y.D. Luo, L.L. Li, B. Gao, H.Q. Wan, L. Dong, Advantageous interfacial effects of AgPd/g-C_3N_4 for photocatalytic hydrogen evolution: electronic structure and H_2O dissociation, Chem. Eur. J. 25 (19) (2019) 5058–5064.
[49] Y. Cong, J. Zhang, F. Chen, M. Anpo, Synthesis and characterization of nitrogen-doped TiO_2 nanophotocatalyst with high visible light activity, J. Phys. Chem. C. 111 (2007) 6976–6982.
[50] X. Li, Q. Xie, Z. Tian, A. DFT, study of electronic structures and optical properties of nickel, nitrogen doped rutile TiO_2, Chem. Phys. Lett. 710 (2018) 143–146.
[51] C.Z. Zhu, Y.T. Wang, Z.F. Jiang, A.N. Liu, Y. Pu, Q.M. Xian, W.X. Zou, C. Sun, Ultrafine Bi_3TaO_7 nanodot-decorated V, N codoped TiO_2 nanoblocks for visible-light photocatalytic activity: interfacial effect and mechanism insight, ACS Appl. Mater. Interfaces 11 (2019) 13011–13021.
[52] J.Z. Cao, Z.M. Xu, Y. Chen, S.J. Li, Y. Jiang, L.L. Bai, H. Yu, H.X. Li, Z.F. Bian, Tailoring the asymmetric structure of NH_2-UiO-66 metal-organic frameworks for light-promoted selective and efficient gold extraction and separation, Angew. Chem. Int. Ed. 62 (2022), e202302202.
[53] Q.Y. Qiao, Y. Chen, Y. Wang, Y.Q. Ren, J.Z. Cao, F.J. Huang, Z.F. Bian, Surface modification of phosphate ion to promote photocatalytic recovery of precious metals, Chin. Chem. Lett. 34 (2023), 107394.
[54] Y. Pu, Y.D. Luo, X.Q. Wei, J.F. Sun, L.L. Li, W.X. Zou, L. Dong, Synergistic effects of Cu_2O-decorated CeO_2 on photocatalytic CO_2 reduction: surface Lewis acid/base and oxygen defect, Appl. Catal. B Environ. 254 (2019) 580–586.
[55] J. Zhong, Y. Zeng, M. Zhang, W. Feng, D. Xiao, J. Wu, P. Chen, M. Fu, D. Ye, Toluene oxidation process and proper mechanism over Co_3O_4 nanotubes: investigation through in-situ DRIFTS combined with PTR-TOF-MS and quasi in-situ XPS, Chem. Eng. J. 397 (2020), 125375.
[56] L. Long, J. Zhao, L. Yang, M. Fu, J. Wu, B. Huang, D. Ye, Room temperature catalytic ozonation of toluene over MnO_2/Al_2O_3, Chin. J. Catal. 32 (6) (2011) 904–916.
[57] X. Zhang, X. Shi, Q. Zhao, Y. Li, J. Wang, Y. Yang, F. Bi, J. Xu, N. Liu, Defects controlled by acid-modulators and water molecules enabled UiO-67 for exceptional toluene uptakes: an experimental and theoretical study, Chem. Eng. J. 427 (2022) 131573–131586.
[58] L. Chen, W. Cui, J. Li, H. Wang, X.A. Dong, P. Chen, Y. Zhou, F. Dong, The high selectivity for benzoic acid formation on $Ca_2Sb_2O_7$ enables efficient and stable toluene mineralization, Appl. Catal. B Environ. 271 (2020), 118948.
[59] Z. Shayegan, C.S. Lee, F. Haghighat, TiO_2 photocatalyst for removal of volatile organic compounds in gas phase-a review, Chem. Eng. J. 334 (2018) 2408–2439.
[60] J. Li, H. Na, X. Zeng, T. Zhu, Z. Liu, In situ DRIFTS investigation for the oxidation of toluene by ozone over Mn/HZSM-5, Ag/HZSM-5 and Mn–Ag/HZSM-5 catalysts, Appl. Surf. Sci. 311 (2014) 690–696.
[61] F.K. Bi, S.T. Ma, B. Gao, Y. Yang, L.X. Wang, F.H. Fei, J.C. Xu, Y.D. Huang, M. H. Wu, X.D. Zhang, Non-oxide supported Pt-metal-group catalysts for efficiently CO and toluene co-oxidation: difference in water resistance and degradation intermediates, Fuel 344 (2023), 128147.